Progress In Electromagnetics Research, PIER 79, 367–386, 2008

A NONDESTRUCTIVE TECHNIQUE FOR DETERMINING COMPLEX PERMITTIVITY AND PERMEABILITY OF MAGNETIC SHEET MATERIALS USING TWO FLANGED RECTANGULAR WAVEGUIDES

M. W. Hyde IV and M. J. Havrilla

Air Force Institute of Technology
Wright-Patterson AFB
OH 45433-7765, USA

Abstract—In this paper, a nondestructive technique for determining the complex permittivity and permeability of magnetic sheet materials using two flanged rectangular waveguides is presented. The technique extends existing single probe methods by its ability to simultaneously measure reflection and transmission coefficients imperative for extracting both permittivity and permeability over all frequencies. Using Love's Equivalence Principle, a system of coupled magnetic field integral equations (MFIEs) is formed. Evaluation of one of the two resulting spectral domain integrals via complex plane integration is discussed. The system, solved via the Method of Moments (MoM), yields theoretical values for the reflection and transmission coefficients. These values are compared to measured values and the error minimized using nonlinear least squares to find the complex permittivity and permeability of a material. Measurement results for two magnetic materials are presented and compared to traditional methods for the purpose of validating the new technique. The technique's sensitivity to uncertainties in material thickness and waveguide alignment is also examined.

1. INTRODUCTION

Waveguide probes, whether coaxial, rectangular, or circular, have been extensively researched. Existing applications of waveguide probes include subsurface crack detection; electromagnetic characterization of materials, especially liquids and biological tissue; and microwave hyperthermia treatment [1–19]. Nearly all published waveguide probe

research focuses on obtaining the reflection coefficient, using a single probe, from an unknown material. While this arrangement is perfect for nondestructively determining complex permittivity of an unknown dielectric, it fails when one wants to fully characterize a magnetic material. Several researchers have developed methods — two thickness method, frequency varying method, and sample added method — to overcome this shortfall; however, these techniques are not always applicable [15–19]. A suitable alternative would be a system which allows the measurement of reflection and transmission coefficients since such measurements are independent over all wavelengths and are the most efficient means of simultaneously determining permittivity and permeability [20]. The focus of this paper is the development of such a system.

In order to fully characterize a planar layer of material, theoretical expressions for the reflection and transmission coefficients must be found. Figure 1 shows the structure analyzed in this paper. Using

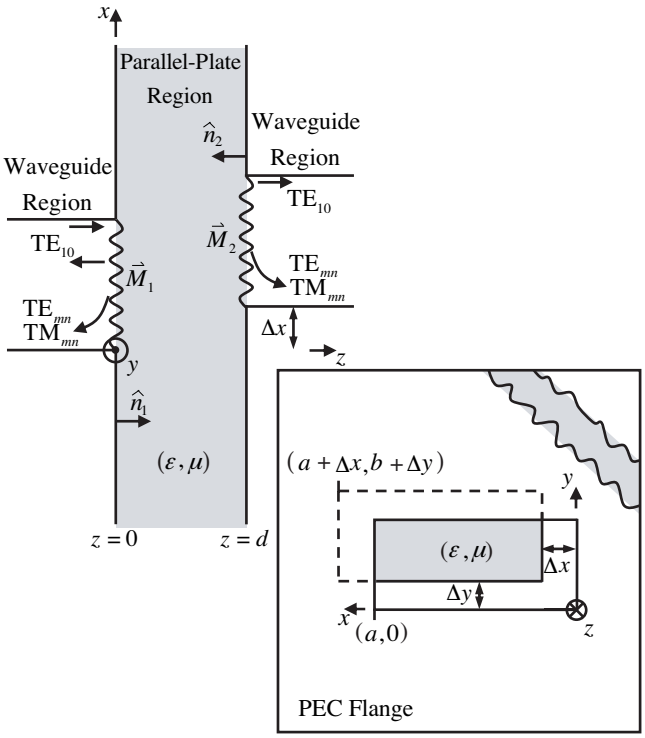

Figure 1. Side (top) and top (bottom) views of the flanged waveguides measurement geometry.

Love's Equivalence Principle, the waveguide apertures in Figure 1 can be replaced with equivalent magnetic currents emanating in a parallel-plate environment [21, 22]. Making use of these currents and the parallel-plate Green's function, one can find an expression for the magnetic field in the parallel-plate region. Enforcing the continuity of tangential fields at the waveguide apertures produces a system of coupled MFIEs, which when solved via the MoM [22], yields theoretical values for the reflection and transmission coefficients. These theoretical values can then be compared to measured data and the system optimized via nonlinear least squares to yield complex permittivity and permeability values.

In this paper, a thorough analysis of Figure 1 will be presented, including the development of the system of coupled MFIEs and spectral domain integration via complex plane analysis. Lastly, measurement results of two magnetic materials comparing the flanged waveguides technique to standard waveguide methods [23, 24] will be shown. Included in these measurement results will be the technique's sensitivity to probe misalignment and sample thickness.

2. DERIVATION AND SOLUTION OF COUPLED MAGNETIC FIELD INTEGRAL EQUATIONS

Material characterization requires one to solve forward and inverse problems. The forward problem involves finding theoretical expressions for the reflection and transmission coefficients; whereas, the inverse problem involves finding the complex permittivity and permeability, by some means, using the results of the forward problem. In very rare instances closed-form expressions can be found that directly relate the forward and inverse problems, i.e., relate complex permittivity and permeability to reflection and transmission coefficients [23, 24]. In most cases (including the one presented in this paper), the inverse problem is solved using numerical techniques such as Newton's method or nonlinear least squares. The purpose of the next two sections will be to solve the forward problem.

Consider the measurement geometry shown in Figure 1. In order to find theoretical expressions for the reflection, Γ, and transmission, T, coefficients, one must find expressions for the electric and magnetic fields in the waveguide and parallel-plate regions. The transverse fields in the waveguide regions take the form of transverse electric (TE) and

transverse magnetic (TM) rectangular waveguide modes:

$$\begin{aligned}\vec{E}^{\,t} &= \vec{e}_{10}e^{-\gamma_{10}z} + \sum_m \sum_n \Gamma_{mn}\vec{e}_{mn}e^{\gamma_{mn}z} \\ \vec{H}^{\,t} &= \vec{h}_{10}e^{-\gamma_{10}z} - \sum_m \sum_n \Gamma_{mn}\vec{h}_{mn}e^{\gamma_{mn}z}\end{aligned} \tag{1}$$

when $z < 0$ and

$$\begin{aligned}\vec{E}^{\,t} &= \sum_m \sum_n \mathrm{T}_{mn}\vec{e}_{mn}e^{-\gamma_{mn}(z-d)} \\ \vec{H}^{\,t} &= \sum_m \sum_n \mathrm{T}_{mn}\vec{h}_{mn}e^{-\gamma_{mn}(z-d)}\end{aligned} \tag{2}$$

when $z > d$ [21]. In (1) and (2), $\vec{e}_{mn}$ and $\vec{h}_{mn}$ are the transverse modal distributions of the electric and magnetic field, respectively; they are shown in the appendix. If the waveguides in Figure 1 are perfectly aligned, only higher order modes with symmetric distributions about the center of the waveguides ($m = 1, 3, 5, \ldots$; $n = 0, 2, 4, \ldots$) will be generated. This is due to the symmetry of the TE_{10} incident field and the structure. On the other hand, if the waveguides in Figure 1 are misaligned, all higher order modes, with the exception of TE_{0n} modes, will be generated.

The transverse fields in the parallel-plate region of Figure 1 can be found by replacing the waveguide apertures with equivalent magnetic currents, $\vec{M}_1$ and $\vec{M}_2$ [21, 22]. Using the parallel-plate Green's function and the electric vector potential, the transverse magnetic field can be found from the following expression

$$\vec{H}^{\,t} = \frac{1}{j\omega\mu\varepsilon}\left(k^2 + \nabla_t\nabla\cdot\right)\vec{F} \tag{3}$$

where the electric vector potential, $\vec{F}$, is

$$\begin{aligned}\vec{F} \;=\; & \int_0^b \int_0^a \overleftrightarrow{G}\left(x, y, z|x', y', 0\right)\cdot\varepsilon\vec{M}_1\left(x', y'\right)dx'dy' \\ & + \int_{\Delta y}^{b+\Delta y}\int_{\Delta x}^{a+\Delta x} \overleftrightarrow{G}\left(x, y, z|x', y', d\right)\cdot\varepsilon\vec{M}_2\left(x', y'\right)dx'dy',\end{aligned} \tag{4}$$

$k = \omega\sqrt{\mu\varepsilon}$ is the material's complex-valued wavenumber, and ∇_t is the transverse gradient operator. In (4), $\overleftrightarrow{G}$ is the dyadic, parallel-plate

Green's function derived in [25, 26]:

$$\begin{aligned}
\overleftrightarrow{G} &= \hat{x}G^t\hat{x} + \hat{y}G^t\hat{y} + \hat{z}G^n\hat{z} \\
G^t_n &= \frac{1}{(2\pi)^2}\int_{-\infty}^{\infty}\int_{-\infty}^{\infty}\tilde{G}^t_n\left(\xi,\eta,z|z'\right)e^{j\xi(x-x')}e^{j\eta(y-y')}d\xi d\eta \\
\tilde{G}^t_n &= \frac{\cosh p\left(d-|z-z'|\right) \pm \cosh p\left(d-(z+z')\right)}{2p\sinh pd}
\end{aligned} \tag{5}$$

where G^t and G^n represent the transverse and normal components of the Green's function, respectively, and $p = \sqrt{\xi^2+\eta^2-k^2}$ is the spectral domain, z-directed wavenumber [4].

With expressions for the fields in the waveguide and parallel-plate regions of Figure 1, a system of coupled MFIEs can be formed by enforcing the continuity of transverse magnetic fields at the waveguide apertures. Setting the transverse magnetic fields of (1) and (2) equal to (3) at $z = 0$ and $z = d$, respectively, results in the desired coupled MFIEs:

$$\begin{aligned}
&\vec{h}_{10} - \sum_m\sum_n \Gamma_{mn}\vec{h}_{mn} = \frac{1}{j\omega\mu}\left(k^2+\nabla_t\nabla\cdot\right) \\
&\left[\int_{s_1}\overleftrightarrow{G}\left(z=0|z'=0\right)\cdot\vec{M}_1 ds' + \int_{s_2}\overleftrightarrow{G}\left(z=0|z'=d\right)\cdot\vec{M}_2 ds'\right] \\
&\sum_m\sum_n \mathrm{T}_{mn}\vec{h}_{mn} = \frac{1}{j\omega\mu}\left(k^2+\nabla_t\nabla\cdot\right) \\
&\left[\int_{s_1}\overleftrightarrow{G}\left(z=d|z'=0\right)\cdot\vec{M}_1 ds' + \int_{s_2}\overleftrightarrow{G}\left(z=d|z'=d\right)\cdot\vec{M}_2 ds'\right]
\end{aligned} \tag{6}$$

where s_1 and s_2 have been introduced to represent the limits of integration in (4).

Solving (6) for Γ and T can be accomplished via the MoM. The first step in the MoM is to choose suitable basis functions to represent the unknown currents. $\vec{M}_1$ and $\vec{M}_2$ in (6) are related to the transverse electric fields at the waveguide apertures by the following expressions

$$\begin{aligned}
\vec{M}_1 &= -\hat{n}_1\times\vec{E}^{ap}(z=0) = -\hat{z}\times\vec{E}^{ap}(z=0) \\
\vec{M}_2 &= -\hat{n}_2\times\vec{E}^{ap}(z=d) = \hat{z}\times\vec{E}^{ap}(z=d)
\end{aligned}. \tag{7}$$

Since the transverse electric fields must be equal across each aperture interface, it is logical to substitute the electric field expressions of (1)

and (2) into (7) resulting in the following expressions for $\vec{M}_1$ and $\vec{M}_2$

$$\begin{aligned} \vec{M}_1 &= -\hat{z} \times \left[\vec{e}_{10} + \sum_m \sum_n \Gamma_{mn} \vec{e}_{mn} \right] \\ \vec{M}_2 &= \hat{z} \times \left[\sum_m \sum_n \mathrm{T}_{mn} \vec{e}_{mn} \right] \end{aligned} . \tag{8}$$

Substituting (8) into (6) results in a system of 2 equations and 2N unknowns. To make the system well defined, testing functions must be chosen (the last step in the MoM) and applied to (6). The choice of testing functions is somewhat subjective; however, in this case, it makes sense to test with $\vec{h}_{mn}$ to take advantage of the orthogonal properties of the waveguide modes. Application of the testing function $\vec{h}_{mn}$ and subsequent integration over the guide cross section results in a 2N by 2N matrix equation, $Ax = b$, where the matrix A is the impedance matrix, x is a vector containing the unknown modal reflection and transmission coefficients, and b is a vector containing the incident field excitation. Inspection of A reveals the following form

$$\begin{bmatrix} A^{11}_{10,10} & \cdots & A^{11}_{10,mn} & A^{12}_{10,10} & \cdots & A^{12}_{10,mn} \\ \vdots & \ddots & \vdots & \vdots & \ddots & \vdots \\ A^{11}_{\tilde{m}\tilde{n},10} & \cdots & A^{11}_{\tilde{m}\tilde{n},mn} & A^{12}_{\tilde{m}\tilde{n},10} & \cdots & A^{12}_{\tilde{m}\tilde{n},mn} \\ A^{21}_{10,10} & \cdots & A^{21}_{10,mn} & A^{22}_{10,10} & \cdots & A^{22}_{10,mn} \\ \vdots & \ddots & \vdots & \vdots & \ddots & \vdots \\ A^{21}_{\tilde{m}\tilde{n},10} & \cdots & A^{21}_{\tilde{m}\tilde{n},mn} & A^{22}_{\tilde{m}\tilde{n},10} & \cdots & A^{22}_{\tilde{m}\tilde{n},mn} \end{bmatrix} \tag{9}$$

where the submatrix A^{11} represents a "self" term, i.e., the source and observer are at $z = 0$. Likewise, A^{22} is also a "self" term — source and observer are at $z = d$. The off-diagonal submatrices, A^{12} and A^{21}, are "coupling" terms. They describe how a source at $z = d$ influences the fields at $z = 0$, A^{12}, and vice versa, A^{21}. Submatrices A^{12} and A^{21} are found to be equal as expected by reciprocity. It is also found that A^{11} and A^{22} are equal, regardless of waveguide misalignment, as anticipated by symmetry. The subscript of each submatrix element describes how a certain waveguide mode couples into another. For example, the $\tilde{m}\tilde{n}, mn$ elements describe how the mnth source mode couples into the $\tilde{m}\tilde{n}$th field mode.

In the next section, it is shown how complex plane integration can be utilized in evaluating the matrix elements in (9). By using the spectral domain representation of the parallel-plate Green's function,

closed-form solutions to all spatial integrals in (6) and an infinite series representation of one of the spectral integrals in (5) are obtained which greatly accelerate convergence and enhance physical insight. For the sake of brevity, only the evaluation of the $A^{12}_{\tilde{m}0,m0}$ elements is demonstrated.

3. SPECTRAL DOMAIN INTEGRATION

In the previous section, the forward problem for the measurement geometry in Figure 1 was introduced. Analysis ultimately led to a system of coupled MFIEs for the modal reflection and transmission coefficients. Applying the MoM to the system of MFIEs resulted in a matrix equation, $Ax = b$, where A was the impedance matrix, x was a vector containing the unknown modal reflection and transmission coefficients, and b was a vector containing the incident field. This section will complete the forward problem of Figure 1 by calculating the $A^{12}_{\tilde{m}0,m0}$ elements of the impedance matrix. This class of elements provides an excellent example of the role waveguide misalignment plays in the integration. The remaining elements of the impedance matrix can be evaluated in an analogous manner.

The impedance matrix elements, $A^{12}_{\tilde{m}0,m0}$, have the following form

$$A^{12}_{\tilde{m}0,m0} = \frac{m\pi/a}{j\omega\mu\left(2\pi\right)^2} \int\limits_{-\infty}^{\infty}\int\limits_{-\infty}^{\infty} \frac{\left(k^2-\xi^2\right)}{p\sinh pd} f_{\tilde{m}0}(\xi,\eta) g_{m0}(\xi,\eta) d\eta d\xi \quad (10)$$

where

$$\begin{aligned} f_{\tilde{m}0}(\xi,\eta) &= \int\limits_0^a \sin\left(\frac{\tilde{m}\pi x}{a}\right) e^{j\xi x} dx \int\limits_0^b e^{j\eta y} dy \\ g_{m0}(\xi,\eta) &= \int\limits_{\Delta x}^{a+\Delta x} \sin\frac{m\pi}{a}\left(x'-\Delta x\right) e^{-j\xi x'} dx' \int\limits_{\Delta y}^{b+\Delta y} e^{-j\eta y'} dy' \end{aligned} \quad . \quad (11)$$

The spatial integrals in (11) can be evaluated in closed-form and are shown in the appendix. Substituting the results of (11) into (10)

produces the following expression

$$A^{12}_{\tilde{m}0,m0} = \frac{\tilde{m}m^2\pi^3/a^3}{j\omega\mu\left(2\pi\right)^2} \int\limits_{-\infty}^{\infty}\left(k^2-\xi^2\right)\frac{\left(1+(-1)^{m+1}\,e^{-j\xi a}\right)\left(1+(-1)^{\tilde{m}+1}\,e^{j\xi a}\right)e^{-j\xi\Delta x}}{\left(\xi^2-\left(m\pi/a\right)^2\right)\left(\xi^2-\left(\tilde{m}\pi/a\right)^2\right)} \int\limits_{-\infty}^{\infty}\frac{e^{-j\eta\Delta y}}{p\sinh pd}\frac{\left(1-e^{-j\eta b}\right)\left(1-e^{j\eta b}\right)}{\eta^2}d\eta d\xi \quad . \tag{12}$$

Inspection of the η integrand in (12) yields a double pole at $\eta = 0$ and simple poles at $\eta = \pm\sqrt{k^2-\xi^2-\left(\ell\pi/d\right)^2}$ $(\ell = 0, 1, 2, \ldots)$. The double pole at $\eta = 0$ comes from a combination of the TE_{m0} basis and $\mathrm{TE}_{\tilde{m}0}$ testing functions. If the y-directed waveguide misalignment is zero ($\Delta y = 0$), this double pole becomes a simple pole since the structure in Figure 1 becomes perfectly symmetric in y. The simple poles at $\eta = \pm\sqrt{k^2-\xi^2-\left(\ell\pi/d\right)^2}$ are a result of the Green's function and physically represent the natural modes of the parallel-plate region. Because the η integrand is even in $p = \sqrt{\xi^2+\eta^2-k^2}$, the branch points, $\eta = \pm\sqrt{k^2-\xi^2}$, and associated branch cut contributions are removable [4]. This result is intuitive since the infinite parallel-plate structure in Figure 1 is closed and consequently non-radiating [4]. Expanding the product in the η integrand produces the following integral

$$\int\limits_{-\infty}^{\infty}\frac{e^{-j\eta\Delta y}}{p\sinh pd}\frac{\left(1-e^{-j\eta b}\right)\left(1-e^{j\eta b}\right)}{\eta^2}d\eta = \int\limits_{-\infty}^{\infty}\frac{1}{p\sinh pd}\frac{2e^{-j\eta\Delta y}-e^{-j\eta b}e^{-j\eta\Delta y}-e^{j\eta b}e^{-j\eta\Delta y}}{\eta^2}d\eta \quad . \tag{13}$$

To ensure convergence of (13), proper integration contours must be chosen. Letting $\eta = \eta_{re} + j\eta_{im}$, reveals that the magnitude and sign of the y-directed waveguide misalignment (Δy) are extremely important. For instance, if $\Delta y > b$, then lower half plane (LHP) closure is required to ensure (13) converges; however, if $0 < \Delta y < b$, then a combination of LHP and upper half plane (UHP) closure is required. Since the former represents an extreme misalignment case, certainly noticeable to the unaided eye, it will not be investigated. The remainder of this

section will deal with the latter case, $0 < \Delta y < b$, since it presents a much more realistic misalignment scenario. Under the assumption that $0 < \Delta y < b$, (13) should be split into the following two integrals

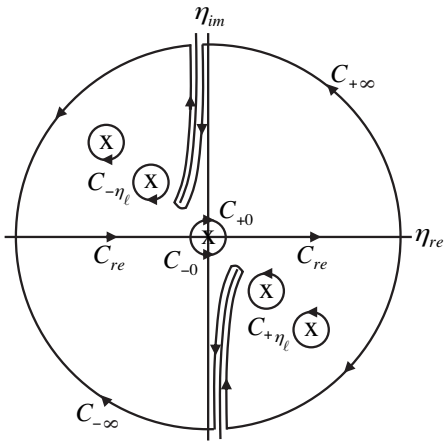

Figure 2. Complex η-plane (branch cuts are removable).

$$\begin{aligned}
&\int_{-\infty}^{\infty} \frac{1}{p\sinh pd} \frac{2e^{-j\eta\Delta y} - e^{-j\eta b}e^{-j\eta\Delta y} - e^{j\eta b}e^{-j\eta\Delta y}}{\eta^2} d\eta = \\
&\int_{-\infty}^{\infty} \frac{1}{p\sinh pd} \frac{-e^{j\eta b}e^{-j\eta\Delta y}}{\eta^2} d\eta + \int_{-\infty}^{\infty} \frac{1}{p\sinh pd} \frac{2 - e^{-j\eta b}}{\eta^2} e^{-j\eta\Delta y} d\eta
\end{aligned} \tag{14}$$

where the first integral in (14) requires UHP closure and the second LHP closure. Figure 2 shows the complex η-plane complete with the appropriate integration contours. Using Cauchy's Integral Theorem and Jordan's Lemma, $\int\limits_{C_{\pm\infty}} = 0$, (14) becomes

$$\begin{aligned}
&\int_{-\infty}^{\infty} \frac{1}{p\sinh pd} \frac{-e^{j\eta b}e^{-j\eta\Delta y}}{\eta^2} d\eta = \int_{C_{re}} = -\int_{C_{+0}} - \sum_{\ell=0}^{\infty} \oint_{C_{-\eta_\ell}} \\
&\int_{-\infty}^{\infty} \frac{1}{p\sinh pd} \frac{2 - e^{-j\eta b}}{\eta^2} e^{-j\eta\Delta y} d\eta = \int_{C_{re}} = -\int_{C_{-0}} - \sum_{\ell=0}^{\infty} \oint_{C_{+\eta_\ell}}
\end{aligned} \tag{15}$$

where $C_{\pm 0}$ are semi-circular contours around the double pole at $\eta = 0$ [27]. By utilizing Cauchy's Integral Formula and the following residue

formulas [27]

$$\begin{aligned} a_{-1} &= \frac{1}{(m-1)!}\frac{\partial^{m-1}}{\partial z^{m-1}}\left[(z-z_0)^m f(z)\right]_{z=z_0} \\ a_{-1} &= \frac{f_1(z_0)}{f_2'(z_0)} \end{aligned}, \tag{16}$$

(13) becomes

$$\begin{aligned} &\int_{-\infty}^{\infty} \frac{e^{-j\eta\Delta y}}{p\sinh pd}\frac{\left(1-e^{-j\eta b}\right)\left(1-e^{j\eta b}\right)}{\eta^2}d\eta = 2\pi(b-\Delta y)\frac{1}{p_0\sinh p_0 d} \\ &-\frac{j4\pi}{d}\sum_{\ell=0}^{\infty}\frac{e^{-j\eta_\ell\Delta y}-e^{-j\eta_\ell b}\cos\eta_\ell\Delta y}{\eta_\ell^3(-1)^\ell(1+\delta_{\ell,0})} \end{aligned} . \tag{17}$$

$$p_0=\sqrt{\xi^2-k^2},\ \eta_\ell=\sqrt{k^2-\xi^2-(\ell\pi/d)^2},\ \delta_{\ell,0}=\begin{cases}1 & \ell=0\\ 0 & \ell\neq 0\end{cases}$$

Note that the parallel-plate mode poles η_ℓ become branch points in the ξ-plane resulting in irremovable branch cut contributions [4]. It is for this reason that the ξ integral is calculated numerically using real-axis integration instead of Cauchy's Integral Theorem. It is worth noting that the integral can be simplified for numerical computation by taking advantage of the evenness of the integrand. It can be easily shown that when $\tilde{m}+1$ and $m+1$ sum to an even number, (12) simplifies to

$$\begin{aligned} A^{12}_{\tilde{m}0,m0} &= \frac{\tilde{m}m^2\pi^3/a^3}{j\omega\mu 2\pi^2} \\ &\int_0^{\infty}\left(k^2-\xi^2\right)\frac{\left(1+(-1)^{m+1}e^{-j\xi a}\right)\left(1+(-1)^{\tilde{m}+1}e^{j\xi a}\right)\cos\xi\Delta x}{\left(\xi^2-(m\pi/a)^2\right)\left(\xi^2-(\tilde{m}\pi/a)^2\right)} \\ &\left[2\pi(b-\Delta y)\frac{1}{p_0\sinh p_0 d}-\frac{j4\pi}{d}\sum_{\ell=0}^{\infty}\frac{e^{-j\eta_\ell\Delta y}-e^{-j\eta_\ell b}\cos\eta_\ell\Delta y}{\eta_\ell^3(-1)^\ell(1+\delta_{\ell,0})}\right]d\xi \end{aligned} . \tag{18}$$

Similarly, when $\tilde{m}+1$ and $m+1$ sum to an odd number, (12) reduces

to

$$A^{12}_{\tilde{m}0,m0} = \frac{-\tilde{m}m^2\pi^3/a^3}{\omega\mu 2\pi^2} \int_0^\infty \left(k^2-\xi^2\right) \frac{\left(1+(-1)^{m+1}\,e^{-j\xi a}\right)\left(1+(-1)^{\tilde{m}+1}\,e^{j\xi a}\right)\sin\xi\Delta x}{\left(\xi^2-(m\pi/a)^2\right)\left(\xi^2-(\tilde{m}\pi/a)^2\right)} \cdot \left[2\pi\,(b-\Delta y)\,\frac{1}{p_0\sinh p_0 d} - \frac{j4\pi}{d}\sum_{\ell=0}^{\infty}\frac{e^{-j\eta_\ell\Delta y}-e^{-j\eta_\ell b}\cos\eta_\ell\Delta y}{\eta_\ell^3\,(-1)^\ell\,(1+\delta_{\ell,0})}\right] d\xi \tag{19}$$

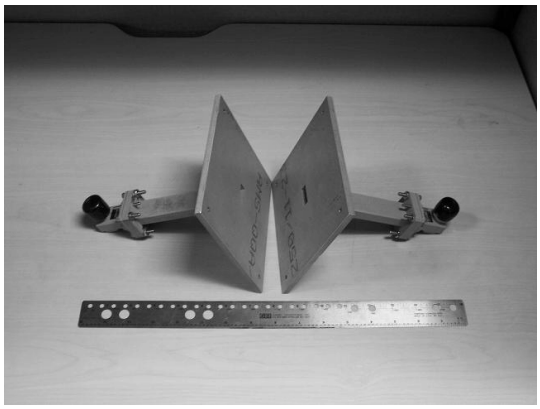

Figure 3. $6'' \times 6'' \times 0.25''$ aluminum flanges attached to X-band rectangular waveguides.

4. MEASUREMENT RESULTS

In this section, measurement results will be shown for the nondestructive technique derived in the previous sections. The results will be compared with those returned from traditional destructive waveguide techniques [23, 24]. Figure 3 shows a picture of the measurement apparatus. The flanges were constructed from aluminum and measure approximately $6'' \times 6'' \times 0.25''$. They were attached with screws to X-band rectangular waveguides. The apparatus was calibrated using a thru-reflect-line (TRL) calibration [3]. For this experiment, two lossy, magnetic materials (ECCOSORB® FGM-40 and FGM-125) were measured using an HP 8510C vector network analyzer (VNA). The relative complex permittivity, ε_r, and

permeability, μ_r, values for FGM-40 and FGM-125 were found by solving the following system of equations,

$$\begin{aligned}
\left|S_{11}^{thy}(\varepsilon_r,\mu_r)-S_{11}^{meas}\right| &\le \delta \\
\left|S_{12}^{thy}(\varepsilon_r,\mu_r)-S_{12}^{meas}\right| &\le \delta \\
\left|S_{21}^{thy}(\varepsilon_r,\mu_r)-S_{21}^{meas}\right| &\le \delta \\
\left|S_{22}^{thy}(\varepsilon_r,\mu_r)-S_{22}^{meas}\right| &\le \delta
\end{aligned} \quad , \tag{20}$$

$$S_{11}^{thy}=S_{22}^{thy}=\Gamma_{10},\ S_{12}^{thy}=S_{21}^{thy}=\mathrm{T}_{10}$$

within some tolerance, δ, using nonlinear least squares. It should be noted that while the development shown in the previous sections is applicable to any material, the technique, in practice, should only be used to extract the parameters of lossy materials. This consideration is due to the finite truncation of the flanges in order to make the method practical. Dominant mode propagation in the parallel-plate region of Figure 1 is cylindrical in nature with propagation constant k, i.e.,

$$\left|\vec{E}\right|,\left|\vec{H}\right| \sim \left|H_0^{(2)}(k\rho)\right| \tag{21}$$

where $H_0^{(2)}$ is a zeroth-order Hankel function of the second kind. It is possible to introduce measurement error from detecting waves reflected from the edges of the flanges. Depending on the dynamic range of the VNA used, the cross sectional dimensions of the flanges should be large enough or the material lossy enough to ensure that waves emanating from the waveguide apertures are sufficiently decayed as to approximate infinite flanges. Figure 4 shows the two-way attenuation of the materials measured in this experiment as well as that of acrylic. The dynamic range of the HP 8510C is listed at 90 dB [28]. It is clear from Figure 4 that $6'' \times 6''$ flanges are sufficient to characterize both magnetic materials with negligible two-way reflection error. This, however, is not the case for acrylic. In order to negate any possible two-way reflection error for a low loss material like acrylic, one needs flanges on the order of $200'' \times 200''$.

Complex permittivity and permeability results for FGM-40 are shown in Figure 5. In the figure, the flanged waveguides technique, when 1, 5, and 10 modes are modeled, is compared to standard waveguide extraction methods [23, 24]. The error bars

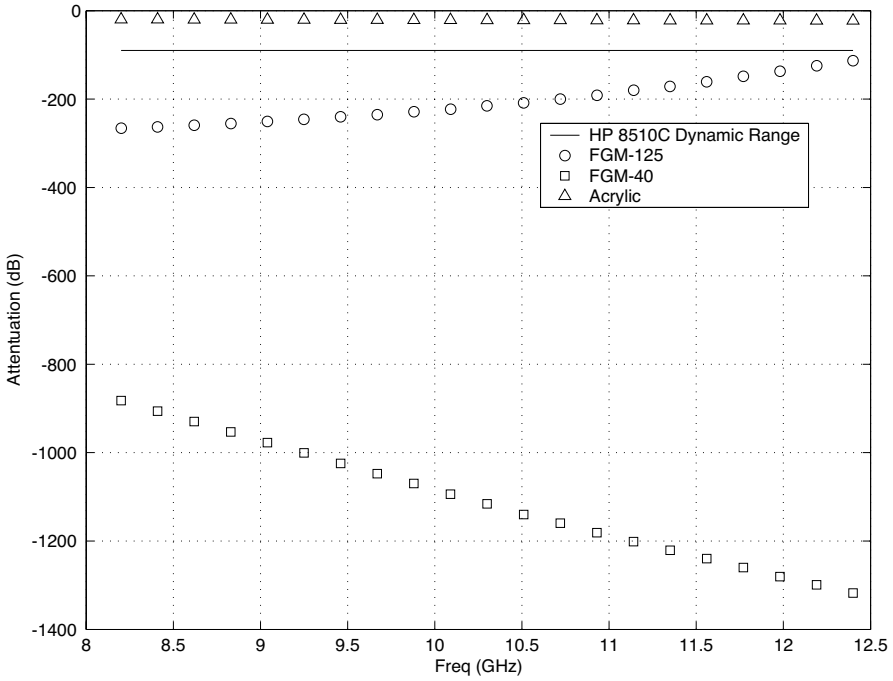

Figure 4. Attenuation of fields propagating to and from the edges of $6'' \times 6''$ PEC flanges filled with FGM-125, FGM-40, and acrylic.

on the waveguide method traces show the effect of a $\pm 0.002''$ material thickness uncertainty; whereas, the error bars on the flanged waveguides technique traces show the combined effect of a $\pm 0.002''$ material thickness uncertainty and a $\pm 0.01''$ waveguide alignment uncertainty. Although both sources of error are combined in the flanged waveguides technique traces, the material thickness uncertainty drives the overall uncertainty. The technique is quite resistant to uncertainty in waveguide alignment even to a large degree. For instance, when accounting for 10 modes, a waveguide alignment uncertainty of $\pm 0.01''$ accounts for an average uncertainty in permittivity and permeability of approximately ± 0.0257. On the other hand, a material thickness uncertainty of $\pm 0.002''$ accounts for an average uncertainty in permittivity and permeability of approximately ± 0.6646, or 26 times greater than that of the waveguide alignment uncertainty. Overall, the flanged waveguides technique does very well when compared to results returned by traditional waveguide methods. Since FGM-40 is a relatively thin material ($\approx 0.040''$), the benefit of

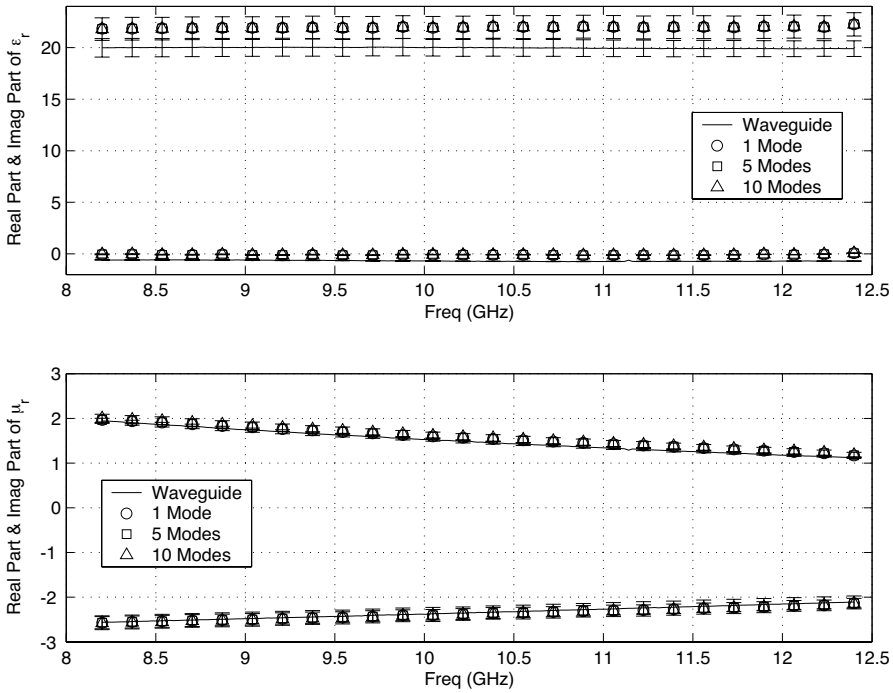

Figure 5. Complex permittivity and permeability results for FGM-40 comparing the flanged waveguides technique to standard waveguide methods. Real parts are positive and imaginary parts are negative.

including higher order modes is not readily apparent. The link between sample thickness and higher order mode contribution will be discussed later.

Figure 6 shows the complex permittivity and permeability results for FGM-125. As in Figure 5, the flanged waveguides technique, when 1, 5, and 10 modes are modeled, is compared to standard waveguide extraction methods [23, 24]. The error bars represent the exact same uncertainties as they did in Figure 5. As before, the flanged waveguide technique does very well when compared to results returned by traditional waveguide methods. Since FGM-125 ($\approx 0.125''$) is roughly three times thicker than FGM-40, the benefit of including higher order modes is apparent.

The link between sample thickness and higher order mode contribution, evident when one compares Figures 5 and 6, deserves attention. Consider once again the structure in Figure 1. As the sample thickness, d, goes to zero, the waveguide apertures move

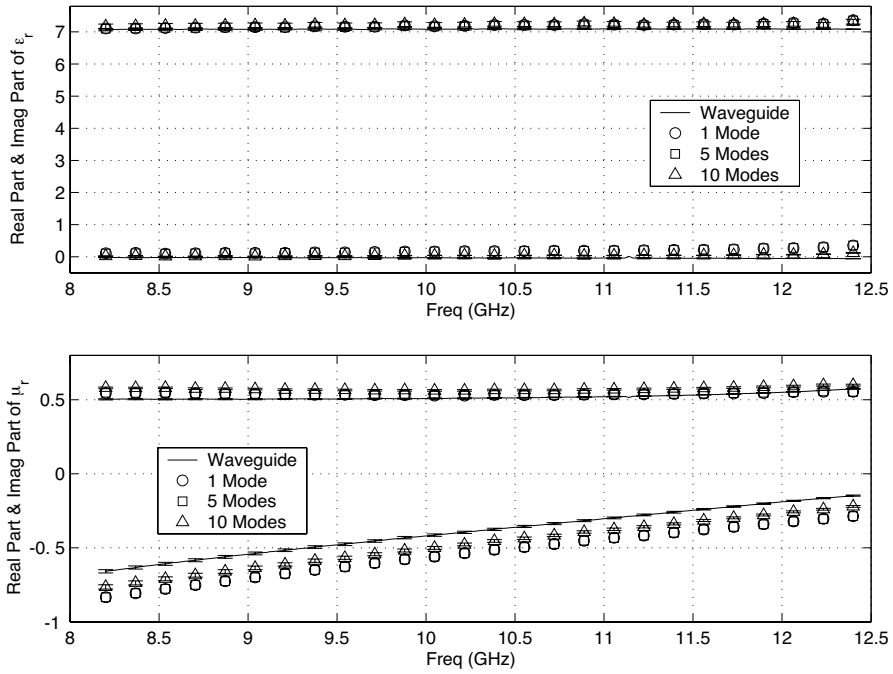

Figure 6. Complex permittivity and permeability results for FGM-125 comparing the flanged waveguides technique to standard waveguide methods. Real parts are positive and imaginary parts are negative.

closer and closer together. At $d = 0$, the apertures merge and the structure behaves like a traditional rectangular waveguide supporting the dominant TE_{10} mode only. Keeping this simple physical picture in mind, it makes sense that the permittivity and permeability of thicker materials would benefit more from the inclusion of higher order modes than that of thinner materials. This is shown experimentally in Figure 7. The figure shows the magnitudes of the first 10 modal reflection coefficients at 10 GHz when the waveguides are misaligned. While both FGM-40 and FGM-125 share a nearly equal reflected TE_{10} mode, the magnitudes of most other higher order modes are significantly greater for FGM-125 than for FGM-40. The most significant higher order mode, as it pertains to permittivity and permeability results, is the TE_{12}/TM_{12} mode pair. The magnitude of FGM-125's TE_{12}/TM_{12} mode pair is approximately three times that of FGM-40's. This is why there is a noticeable difference in FGM-125's permittivity and permeability results when 10 modes are modeled as compared to the same FGM-40 traces.

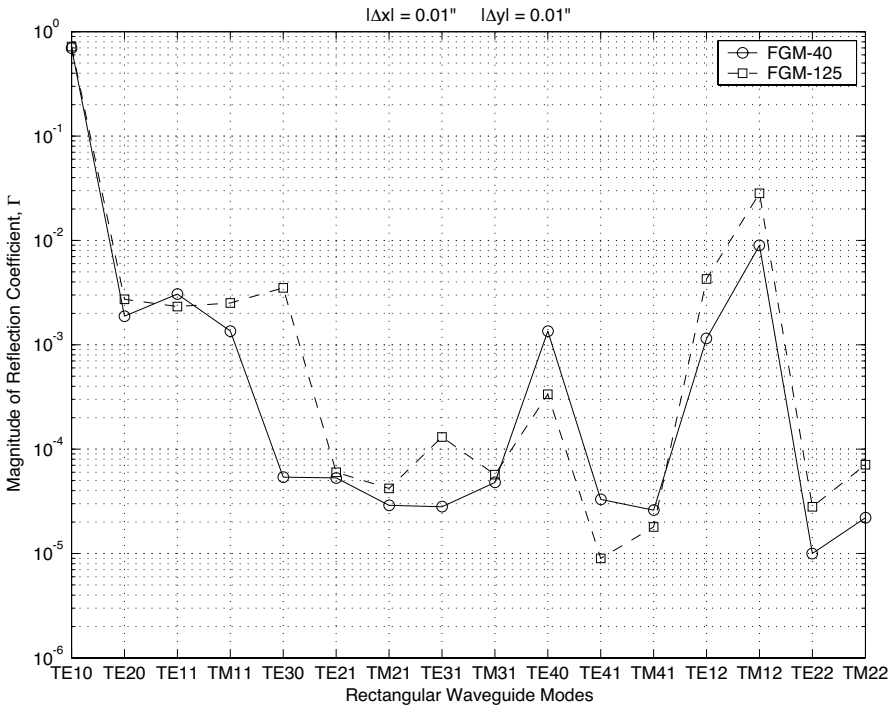

Figure 7. Magnitudes of the first 10 modal reflection coefficients for FGM-40 and FGM-125 at 10 GHz when the waveguides are misaligned. TE and TM modes of the same index are counted as one mode.

5. CONCLUSION

In this paper, a nondestructive technique for determining both complex permittivity and permeability of magnetic sheet materials using two flanged rectangular waveguides was presented. This paper began with a theoretical analysis of the measurement geometry in Figure 1. It was shown that replacing the waveguide apertures with equivalent magnetic currents, in accordance with Love's Equivalence Principle, resulted in a system of coupled MFIEs. This system was then transformed into a matrix equation using the MoM. It was also shown that the spatial integrals of the matrix elements can be evaluated in closed-form and one of the spectral integrals can be represented as an infinite series using complex plane integration. This resulting analysis accelerated convergence and led to enhanced physical insight. Lastly, this paper concluded with experimental results of two magnetic materials comparing the technique to traditional destructive waveguide

methods [23, 24].

The main contribution of the flanged waveguides technique is that it allows for the simultaneous measurement of reflection and transmission coefficients. Since reflection and transmission coefficients are independent over all wavelengths and are the most efficient means of determining both permittivity and permeability of a material, the ability to simultaneously measure these parameters is a major enhancement over existing single probe methods [1–19]. Another beneficial aspect of the flanged waveguides technique is in sample preparation. Compared with traditional waveguide methods, which require samples to be machined, fully-fill the waveguide cross section, and be normal to the guiding axis, the flanged waveguides technique only requires that samples be lossy enough, or the flanges large enough, to ensure negligible two-way reflection error. The flanged waveguides technique's most promising application would be in the RF materials industry. Its ability to nondestructively measure permittivity and permeability of large sheets of magnetic material would be invaluable as a quality assurance tool.

APPENDIX A.

The rectangular waveguide transverse electric, $\vec{e}_{mn}$, and magnetic, $\vec{h}_{mn}$, field distributions are

$$\begin{aligned}
\begin{bmatrix} \vec{e}_{mn}^{\,\mathrm{TE}} \\ \vec{e}_{mn}^{\,\mathrm{TM}} \end{bmatrix} &= \hat{x} \begin{bmatrix} k_y \\ k_x \end{bmatrix} \cos k_x x \sin k_y y + \hat{y} \begin{bmatrix} -k_x \\ k_y \end{bmatrix} \sin k_x x \cos k_y y \\
\begin{bmatrix} \vec{h}_{mn}^{\,\mathrm{TE}} \\ \vec{h}_{mn}^{\,\mathrm{TM}} \end{bmatrix} &= \hat{z} \times \begin{bmatrix} \vec{e}_{mn}^{\,\mathrm{TE}} \Big/ \mathrm{Z}_{mn}^{\mathrm{TE}} \\ \vec{e}_{mn}^{\,\mathrm{TM}} \Big/ \mathrm{Z}_{mn}^{\mathrm{TM}} \end{bmatrix}
\end{aligned} \tag{A1}$$

when $z < 0$ and

$$\begin{aligned}
\begin{bmatrix} \vec{e}_{mn}^{\,\mathrm{TE}} \\ \vec{e}_{mn}^{\,\mathrm{TM}} \end{bmatrix} &= \hat{x} \begin{bmatrix} k_y \\ k_x \end{bmatrix} \cos k_x (x - \Delta x) \sin k_y (y - \Delta y) \\
&\quad + \hat{y} \begin{bmatrix} -k_x \\ k_y \end{bmatrix} \sin k_x (x - \Delta x) \cos k_y (y - \Delta y) \\
\begin{bmatrix} \vec{h}_{mn}^{\,\mathrm{TE}} \\ \vec{h}_{mn}^{\,\mathrm{TM}} \end{bmatrix} &= \hat{z} \times \begin{bmatrix} \vec{e}_{mn}^{\,\mathrm{TE}} \Big/ \mathrm{Z}_{mn}^{\mathrm{TE}} \\ \vec{e}_{mn}^{\,\mathrm{TM}} \Big/ \mathrm{Z}_{mn}^{\mathrm{TM}} \end{bmatrix}
\end{aligned} \tag{A2}$$

when $z > d$. In (A1) and (A2),

$$k_x = \tfrac{m\pi}{a},\ k_y = \tfrac{n\pi}{b},\ \gamma_{mn} = \sqrt{k_x^2 + k_y^2 - k_0^2}$$
$$\mathrm{Z}_{mn}^{\mathrm{TE}} = \tfrac{j\omega\mu_0}{\gamma_{mn}},\ \mathrm{Z}_{mn}^{\mathrm{TM}} = \tfrac{\gamma_{mn}}{j\omega\varepsilon_0} \quad . \tag{A3}$$

The integrals $f_{\tilde{m}0}(\xi,\eta)$ and $g_{m0}(\xi,\eta)$ evaluate to

$$\begin{aligned} f_{\tilde{m}0}(\xi,\eta) &= \int_0^a \sin\left(\frac{\tilde{m}\pi x}{a}\right) e^{j\xi x} dx \int_0^b e^{j\eta y} dy \\ &= \left[\frac{-k_{x\tilde{m}}\left(1+(-1)^{\tilde{m}+1}e^{j\xi a}\right)}{\xi^2 - k_{x\tilde{m}}^2}\right]\left[\frac{j\left(1-e^{j\eta b}\right)}{\eta}\right] \\ g_{m0}(\xi,\eta) &= \int_{\Delta x}^{a+\Delta x} \sin\frac{m\pi}{a}\left(x'-\Delta x\right) e^{-j\xi x'} dx' \int_{\Delta y}^{b+\Delta y} e^{-j\eta y'} dy' \\ &= \left[\frac{-k_{xm}e^{-j\xi\Delta x}\left(1+(-1)^{m+1}e^{-j\xi a}\right)}{\xi^2 - k_{xm}^2}\right]\left[\frac{-je^{-j\eta\Delta y}\left(1-e^{-j\eta b}\right)}{\eta}\right] \end{aligned} \quad . \tag{A4}$$

REFERENCES

1. Li, C. and K. Chen, "Determination of electromagnetic properties of materials using flanged open-ended coaxial probe — Full wave analysis," *IEEE Trans. Instrum. Meas.*, Vol. 44, No. 1, 19–27, Feb. 1995.
2. Chang, C., K. Chen, and J. Qian, "Nondestructive determination of electromagnetic parameters of dielectric materials at X-band frequencies using a waveguide probe system," *IEEE Trans. Instrum. Meas.*, Vol. 46, No. 5, 1084–1092, Oct. 1997.
3. Chen, L. F., C. K. Ong, C. P. Neo, V. V. Varadan, and V. K. Varadan, *Microwave Electronics Measurement and Materials Characterization*, John Wiley & Sons, New York, 2004.
4. Stewart, J. W. and M. J. Havrilla, "Electromagnetic characterization of a magnetic material using an open-ended waveguide probe and a rigorous full-wave multimode model," *Journal of Electromagnetic Waves and Applications*, Vol. 20, No. 14, 2037–2052, 2006.
5. Olmi, R., R. Nesti, G. Pelosi, and C. Riminesi, "Improvement of the permittivity measurement by a 3D full-wave analysis of a

finite flanged coaxial probe," *Journal of Electromagnetic Waves and Applications*, Vol. 18, No. 2, 217–232, 2004.

6. Bois, K. J., A. D. Benally, and R. Zoughi, "Multimode solution for the reflection properties of an open-ended rectangular waveguide radiating into a dielectric half-space: the forward and inverse problems," *IEEE Trans. Instrum. Meas.*, Vol. 48, No. 6, 1131–1140, Dec. 1999.
7. Mautz, J. R. and R. F. Harrington, "Transmission from a rectangular waveguide into half-space through a rectangular aperture," *IEEE Trans. Microwave Theory Tech.*, Vol. MTT-26, No. 1, 44–45, Jan. 1978.
8. Teodoridis, V., T. Sphicopoulos, and F. E. Gardiol, "The reflection from an open-ended rectangular waveguide terminated by a layered dielectric medium," *IEEE Trans. Microwave Theory Tech.*, Vol. MTT-33, No. 5, 359–366, May 1985.
9. Encinar, J. A. and J. M. Rebollar, "Convergence of numerical solutions of open-ended waveguide by modal analysis and hybrid modal-spectral techniques," *IEEE Trans. Microwave Theory Tech.*, Vol. MTT-34, No. 7, 809–814, July 1986.
10. Popovic, D., et al., "Precision open-ended coaxial probes for *in vivo* and *ex vivo* dielectric spectroscopy of biological tissues at microwave frequencies," *IEEE Trans. Microwave Theory Tech.*, Vol. 53, No. 5, 1713–1722, May 2005.
11. Bao, J., S. Lu, and W. D. Hurt, "Complex dielectric measurements and analysis of brain tissues in the radio and microwave frequencies," *IEEE Trans. Microwave Theory Tech.*, Vol. 45, No. 10, 1730–1741, Oct. 1997.
12. Mazlumi, F., S. Sadeghi, and R. Moini, "Interaction of rectangular open-ended waveguides with surface tilted long cracks in metals," *IEEE Trans. Instrum. Meas.*, Vol. 55, No. 6, 2191–2197, Dec. 2006.
13. Huber, C., H. Abiri, S. I. Ganchev, and R. Zoughi, "Modeling of surface hairline-crack detection in metals under coatings using an open-ended rectangular waveguide," *IEEE Trans. Microwave Theory Tech.*, Vol. 45, No. 11, 2049–2057, Nov. 1997.
14. Yeh, C. and R. Zoughi, "A novel microwave method for detection of long surface cracks in metals," *IEEE Trans. Instrum. Meas.*, Vol. 43, No. 5, 719–725, Oct. 1994.
15. Baker-Jarvis, J., M. D. Janezic, P. D. Domich, and R. G. Geyer, "Analysis of an open-ended coaxial probe with lift-off for nondestructive testing," *IEEE Trans. Instrum. Meas.*, Vol. 43, No. 5, 711–718, Oct. 1994.

16. Wang, S., M. Niu, and D. Xu, "A frequency-varying method for simultaneous measurement of complex permittivity and permeability with an open-ended coaxial probe," *IEEE Trans. Microwave Theory Tech.*, Vol. 46, No. 12, 2145–2147, Dec. 1998.
17. Maode, N., S. Yong, Y. Jinkui, F. Chenpeng, and X. Deming, "An improved open-ended waveguide measurement technique on parameters ε_r and μ_r of high-loss materials," *IEEE Trans. Instrum. Meas.*, Vol. 47, No. 2, 476–481, Apr. 1999.
18. Chen, C., Z. Ma, T. Anada, and J. Hsu, "Further study on two-thickness-method for simultaneous measurement of complex EM parameters based on open-ended coaxial probe," *2005 European Microwave Conference*, Paris, France, Oct. 4–6, 2005.
19. Tantot, O., M. Chatard-Moulin, and P. Guillon, "Measurement of complex permittivity and permeability and thickness of multilayered medium by an open-ended waveguide method," *IEEE Trans. Instrum. Meas.*, Vol. 46, No. 2, 519–522, Apr. 1997.
20. Hyde, M. W. and M. J. Havrilla, "Measurement of complex permittivity and permeability using two flanged rectangular waveguides," *2007 International Microwave Symposium*, 531–534, Honolulu, HI., USA, June 3–8, 2007.
21. Collin, R. E., *Field Theory of Guided Waves*, 2nd edition, IEEE Press, New York, 1991.
22. Peterson, A. F., S. L. Ray, and R. Mittra, *Computational Methods for Electromagnetics*, IEEE Press, New York, 1998.
23. Weir, W. B., "Automatic measurement of complex dielectric constant and permeability at microwave frequencies," *Proc. IEEE*, Vol. 62, No. 1, 33–36, Jan. 1974.
24. Nicolson, A. M. and G. F. Ross, "Measurement of the intrinsic properties of materials by time-domain techniques," *IEEE Trans. Instrum. Meas.*, Vol. IM-19, No. 4, 377–382, Nov. 1970.
25. Hanson, G. W. and A. B. Yakovlev, *Operator Theory for Electromagnetics: An Introduction*, Springer-Verlag, New York, 2001.
26. Hanson, G. W., A. I. Nosich, and E. M. Kartchevski, "Green's function expansions in dyadic root functions for shielded layered waveguides," *Progress In Electromagnetics Research*, PIER 39, 61–91, 2003.
27. Arfken, G. B. and H. J. Weber, *Mathematical Methods for Physicists*, 5th ed., Harcourt/Academic Press, New York, 2001.
28. Agilent 8510C Network Analyzer Data Sheet, Agilent Technologies, 2000.